

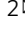


Controlling bimerons as skyrmion analogues by ferroelectric polarization in 2D van der Waals multiferroic heterostructures

Wei Sun ¹, Wenxuan Wang¹, Hang Li ¹✉, Guangbiao Zhang¹, Dong Chen¹, Jianli Wang¹ & Zhenxiang Cheng ²✉

Atom-thick van der Waals heterostructures with nontrivial physical properties tunable via the magnetoelectric coupling effect are highly desirable for the future advance of multiferroic devices. In this work on LaCl/In₂Se₃ heterostructure consisting of a 2D ferromagnetic layer and a 2D ferroelectric layer, reversible switch of the easy axis and the Curie temperature of the magnetic LaCl layer has been enabled by switching of ferroelectric polarization in In₂Se₃. More importantly, magnetic skyrmions in the bimerons form have been discovered in the LaCl/In₂Se₃ heterostructure and can be driven by an electric current. The creation and annihilation of bimerons in LaCl magnetic nanodisks were achieved by polarization switching. It thus proves to be a feasible approach to achieve purely electric control of skyrmions in 2D van der Waals heterostructures. Such nonvolatile and tunable magnetic skyrmions are promising candidates for information carriers in future data storage and logic devices operated under small electrical currents.

¹Institute for Computational Materials Science, School of Physics and Electronics, Henan University, 475004 Kaifeng, People's Republic of China. ²Institute for Superconducting & Electronic Materials, Australian Institute of Innovative Materials, University of Wollongong, Innovation Campus, Squires Way, North Wollongong, NSW 2500, Australia. ✉email: hang.li@vip.henu.edu.cn; cheng@uow.edu.au

A magnetic skyrmion, usually a few nanometers in diameter, is a topologically protected magnetic quasi-particle with a whirling spin texture in real space¹. Stable magnetic skyrmions, emerging in various magnetic materials^{1–6} as a result of competing Heisenberg exchange and Dzyaloshinskii–Moriya interaction (DMI)⁷, can be driven by low current density^{8–13}. The creation and annihilation of magnetic skyrmions in thin films have been demonstrated by current^{14,15}, marking a significant step toward low-dimensional skyrmion systems. In recent experiments skyrmion and its motion under electric current have been observed in Fe₃GeTe₂^{16,17}, proving 2D magnetic materials a new category of skyrmion medium. In addition, another study showed that ferroelectric (FE) polarization can be integrated into the magnetic skyrmion systems to realize nonvolatile control via the magnetoelectric coupling effect in BaTiO₃/SrRuO₃ perovskite heterostructure (HS)¹⁸. It suggests that skyrmions can be controlled directly by electric fields—instead of electric current—via polarization switching. This significantly reduces energy consumption. However, whether this type of control can be extended to atom-thick van der Waals (vdW) HS remains largely elusive. Once achieved, it delivers great application potential for high-performance spintronic devices based on 2D skyrmions.

Since the discovery of graphene, extensive research on two-dimensional ferromagnetic (FM)^{19–25} and FE^{26–32} materials has been carried out rapidly. The magnetic anisotropy in 2D materials induced by spin-orbit coupling enables the long-range magnetic ordering, forming easy-axis or easy-plane 2D magnets. In the easy-axis 2D magnets, skyrmions are usually of the Néel-type, whereas in the easy-plane 2D magnet, skyrmions usually exist in bimerons form^{33–35}. When 2D FE and FM materials are combined to form atomic layer-thick multiferrous vdW HSs, such 2D system endows nonvolatile coupling between two ferroic orderings^{36–38}, compensating the scarcity of the single-phase multiferrous material. Furthermore, nonvolatile FE polarization controlled magnetic skyrmions through the magnetoelectric coupling effect is highly anticipated in such systems. In contrast to the traditional perovskite-based multiferrous HSs, 2D multiferrous HSs have an inherent advantage in achieving strong magnetoelectric coupling, that is, all atoms are exposed to the surface, which makes magnetism more sensitive to FE polarization. Recent reports have demonstrated that the interlayer

magnetolectric coupling in a 2D vdW HSs survives the large space between two different ferroic layers. For example, polarization can manipulate a variety of properties including the conductivity of the CrI₃ in the CrI₃/Sc₂Co₂ HS³⁶, the magnetic anisotropy of the CrGeTe₃ in CrGeTe₃/In₂Se₃ HS³⁷, and magnetic ordering of the FeI₂ in the FeI₂/In₂Se₃ HS³⁸. All these works indicate the possibility of electric control of the magnetism and even skyrmions in 2D vdW HSs.

Although the existence of magnetoelectric coupling effect has been confirmed in the 2D vdW HSs, the influence of the polarization on the magnetism still lacks systematic investigation. Besides, the usual low Curie temperature of the 2D magnetic monolayer limits the study in terms of practical applications. In this work, we propose a LaCl/In₂Se₃ multiferrous HS, where In₂Se₃ is an ideal 2D FE material with controllable out-of-plane spontaneous polarization^{24,39–41}, while LaCl was synthesized decades ago and proved to be a vdW layer compound^{42–45}. Furthermore, LaCl monolayer as an easy-plane FM metal has been confirmed in many works^{46–49}. In addition, La-5*d* orbital has a strong spin-orbit coupling, which satisfies the requirement of producing strong Dzyaloshinskii–Moriya interaction, i.e., a necessary condition for the generation of magnetic chiral skyrmions. The nearly perfect lattice matching (lattice mismatching rate <0.1%) between the two vdW compounds makes them ideal model systems to construct HS for theoretical studies.

Our results show that the magnetic skyrmions in bimerons form is generated in the atom-thick vdW LaCl/In₂Se₃ multiferrous HS, see Fig. 1a, due to the broken inversion symmetry of LaCl by the In₂Se₃ FE polarization. The bimerons can be driven by current and generated or annihilated by FE switching. The diameter of bimeron is only about 23 nm, which enhances the controllability and integrability of the bimerons-based functional devices. In addition, we have systematically investigated the effect of the polarization orientation and magnitude on magnetism and realized the tuning of the Curie temperature and the magnetic easy axis. The strong magnetoelectric coupling effect observed in the 2D HS is unprecedented. Our results pave a new avenue for future devices based on vdW structures.

Results

Material model and computational details. We combined first-principles density functional theory (DFT) and micromagnetic simulation to investigate the magnetism of LaCl monolayer and LaCl/In₂Se₃. Monte Carlo simulation was performed to locate the FM Curie temperature. The electronic properties and basic magnetic parameters of the LaCl monolayer and the LaCl/In₂Se₃ were calculated using the VASP package^{50,51} based on the projected augmented wave (PAW) pseudopotentials. We constructed the HS along the [001] direction, see Fig. 1b, c, fully releasing the *xy*-plane lattice constant and spatial ion coordinates. The lattice constants of the free-standing LaCl and In₂Se₃ monolayer are, respectively, 4.033 Å and 4.035 Å—only 0.1% lattice mismatch rate, and we can thus safely neglect the influence of strain. The Heisenberg type spin Hamiltonian of LaCl can be expressed as,

$$H = -J_1 \sum_{ij} \mathbf{M}_i \cdot \mathbf{M}_j - J_2 \sum_{i,k} \mathbf{M}_i \cdot \mathbf{M}_k - J_3 \sum_{j,l} \mathbf{M}_j \cdot \mathbf{M}_l - D_1 \sum_{ij} \mathbf{M}_i \times \mathbf{M}_j - D_2 \sum_{i,k} \mathbf{M}_i \times \mathbf{M}_k - D_3 \sum_{j,l} \mathbf{M}_j \times \mathbf{M}_l - K \sum_i (M_i^z)^2, \quad (1)$$

where J_1 , J_2 , and J_3 are the exchange coupling parameters; and similar notation applies to the DM vectors (\mathbf{D}_1 , \mathbf{D}_2 , and \mathbf{D}_3), as shown in Fig. 1d. \mathbf{M} denotes the magnetic moment of each atom, and K is the perpendicular magnetic anisotropy constant. The calculation method of the exchange coupling parameter,

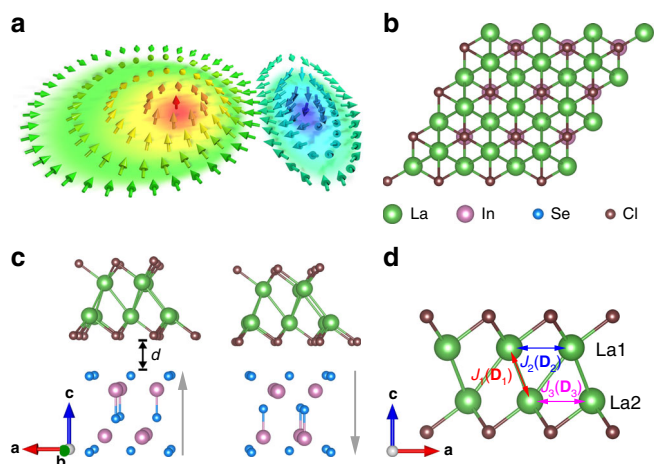


Fig. 1 Crystal structure diagram of LaCl/In₂Se₃ HS. **a** Illustrations of a magnetic bimeron. **b, c** show the top and side views of the HS, respectively. The gray arrow represents the polarization direction of In₂Se₃. **d** Magnetic structure of LaCl for calculating the exchange coupling parameter (DMI vector).

perpendicular magnetic anisotropy constant, and DM vectors are summarized in the Supplementary Information part1 and part2. Subsequently, the parameters extracted from DFT calculation were used subsequently as the input to the micromagnetic simulation using OOMMF software⁵². The boundary effect was taken into account by imposing the interfacial DMI in micromagnetic simulations⁵³.

The skyrmion is defined in terms of the nonzero integer topological charge defined as^{12,54},

$$Q = \frac{1}{4\pi} \int \mathbf{m} \cdot \left(\frac{\partial \mathbf{m}}{\partial x} \times \frac{\partial \mathbf{m}}{\partial y} \right) dx dy, \quad (2)$$

where \mathbf{m} is the normalized magnetization. When Q is quantized at the value ± 1 , we may refer this state to a skyrmion.

In addition, we performed Monte Carlo simulations with a $50 \times 50 \times 1$ supercell based on the Heisenberg model to find the FM Curie temperature (T_c) of the LaCl monolayer and LaCl/In₂Se₃. For each temperature, 10^5 Monte Carlo updates were employed. The FM Curie temperature T_c is estimated by the peak position of the magnetic susceptibility (see Supplementary Information, Part 3).

Micromagnetic simulation of bimeron. Here we use $P+$ ($P-$) to represent the polarization direction of the In₂Se₃ that is along the $+z$ ($-z$) axis. The result shows that the free-standing LaCl monolayer is metallic with in-plane magnetization, consistent with previous reports^{55–57}. In the HS, the interlayer spacing d between LaCl and In₂Se₃ is 3.58 and 3.17 Å in LaCl/ $P+$ and LaCl/ $P-$, respectively, indicating the non-bonded nature. Moreover, both LaCl/ $P+$ and LaCl/ $P-$ structures remain in the metallic FM state, the same as that in the monolayer LaCl, showing that the switching of the In₂Se₃ polarization does not directly affect the magnetic ordering in LaCl. However, the exchange interaction parameters are more sensitive to the polarization. We summarize in Table 1 the calculated exchange interaction parameters. In the $P+$ state, J_2 and J_3 are enhanced compared to that of the free-standing LaCl monolayer, whereas the magnitude of J_1 sees no evident change. Upon polarization reversal to the $P-$ state, J_1 undergoes larger enhancement than J_2 and J_3 . In addition, the FE polarization that originates from the In₂Se₃ layer breaks the spatial inversion symmetry in the adjacent LaCl, which gives rise to a DMI in HS^{7,58}. We present in Table 1 the calculated in-plane \mathbf{D} vector of the HS. The results show that the magnitude of \mathbf{D} vector is different in two polarization states, indicating non-volatile control of the exchange effect and DMI by the FE polarization. The DMI induced in our 2D HS by ferroelectric polarization is superior to the DMI induced in the CrI₃ monolayer by an electric field that breaks its spatial inversion symmetry⁵⁹. In In₂Se₃ the nonvolatile nature of FE polarization persists into the magnetic switching in the LaCl/ $P\pm$ structure with a significant reduction of energy consumption in the proposed device.

We used OOMMF software to perform micromagnetic simulations of the LaCl monolayer and LaCl/ $P\pm$ HSs in a nanodisk geometry with a diameter of 200 nm. The varied

parameters including J , \mathbf{D} , K , and M_s for $P+$ and $P-$ states are listed in Table 1, respectively. The initial spin state was set to paramagnetic (random) states. In the LaCl/ $P+$ configuration, bimerons spin texture emerges, as shown in Fig. 2a. The calculation shows the topological charge of the bimeron $Q = 1.0$, consisting of a vortex ($Q = 0.5$) and an anti-vortex ($Q = 0.5$). The extracted bimeron texture map is depicted in Fig. 2d, e. Due to the presence of in-plane anisotropy, bimeron's outer magnetization is along the in-plane direction rather than the out-of-plane one, which consequently allows two bimerons with opposite topological numbers ($Q = 1$ and $Q = -1$) to coexist in the same magnetic domain (see Supplementary Fig. 4)⁶⁰. This is significantly different from other types of skyrmions. This spin texture disappears, accompanied by a vanishing Q to zero when the polarization is reversed to the $P-$ state, shown in Fig. 2b. Subsequently, we found that bimeron can appear when the K value ranges from -0.04 to -0.13 meV (other parameters remain unchanged). Figure 2c represents the bimeron texture when the $K = -0.1$ meV, showing a smaller bimeron size compared to the $P+$ state and this phenomenon is explained in part 5 of the Supplementary Information. In the $P-$ state, the enhanced K value caused by the polarization completely exceeds the range that allows bimeron to exist, leading to bimeron's annihilation in this polarized state. Furthermore, Fig. 2c verifies the above conclusion that bimerons can appear in the same magnetic domain. Therefore, by simply switching the FE polarization, two distinct magnetic states—referred to in the binary code as “0” and “1”—can be realized and could be used as building blocks for information storage. The diameter of bimeron in LaCl/ $P+$ HS is only about 23 nm, which enhances the controllability and integrability of the bimerons-based functional devices.

We show in Fig. 3 the magnetization as a function of K while keeping other parameters the same as those in the LaCl/ $P+$ configuration. When K is positive, the perpendicular magnetic anisotropy provides an easy axis to support magnetizations pointing either up or down. In this case, the formation of Néel-type skyrmions is energetically favored. When K is negative, however, the easy axis is confined within plane by the in-plane anisotropy, forcing the Néel-type skyrmions to evolve into vortices, the FM stripes into anti-vortices, and eventually the Néel-type skyrmions transform into bimerons.

The current-driven motion of bimeron in the LaCl/ $P+$ configuration was simulated on a 150×600 nm nanotrack. Prior to the injection of current, we created and relaxed the bimeron near the left end of the nanotrack. An in-plane current of $j = 3 \times 10^{10}$ A m⁻² was later applied along the x direction to mobilize the bimeron, see Fig. 2g. The bimeron remains stable while traversing the nanotrack at the speed of 72.17 m s⁻¹; the transverse motion along the y -axis is due to the skyrmion Hall effect^{11,61}.

Regulation of LaCl magnetism by In₂Se₃ polarization. In our system, the out-of-plane polarization of the In₂Se₃ layer redistributes charges in the LaCl layer to screen the polarization field, resulting in a change in the magnetic properties of LaCl. The enhanced polarization is thus expected to improve the regulation for LaCl magnetism. For the ferroelectric substrate In₂Se₃, polarization increases as a function of the film thickness and saturates as the thickness increases to three layers²⁶. Therefore, using a three-layered In₂Se₃, we simulated an enhanced polarization which is denoted as $3P\pm$ for simplicity. Note that the method by increasing the layer thickness for better effect does not apply to all 2D HS system. For example, in the WTe₂/CrI₃ HS, the conductance of WTe₂ depends on the nearest CrI₃ layer and is not affected by the CrI₃ thickness⁶². The impact of the polarization intensity in In₂Se₃ on the magnetism in LaCl is shown in

Table 1 Magnetic parameters of LaCl/In₂Se₃ HS.

	J_1	J_2	J_3	D_1	D_2	D_3	K	M_s
LaCl/ $P+$	1.36	8.32	8.28	0.58	0.78	0.84	-0.19	0.88
LaCl/ $P-$	3.30	5.93	4.92	0.23	0.42	0.31	-0.76	0.93

Summary of exchange coupling parameter (J , in meV), in-plane DM vectors (D , in meV), perpendicular magnetic anisotropy constant (K , in meV), and saturation magnetic moment (M_s , in μ_B).

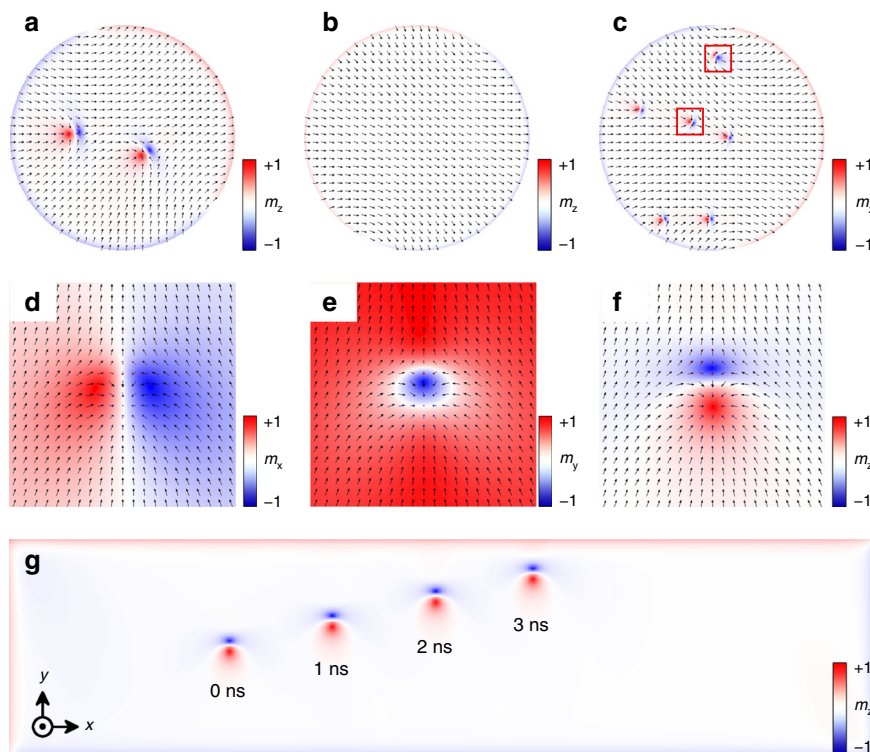


Fig. 2 Ferromagnetic regulation and current drive of bimeron. The top views of the micromagnetic simulation for (a) LaCl/P+ and (b) LaCl/P- HSs. c The top views of the micromagnetic simulation for LaCl/P- HS with $K = -0.1$ meV, the red rectangle shows two bimerons with opposite topological numbers. d-f Blue-red color represents the region of x, y, z component along the magnetic direction of a bimeron. g Snapshots of the bimeron moving under a current of $j = 3 \times 10^{10}$ A m $^{-2}$ on nanotracks.

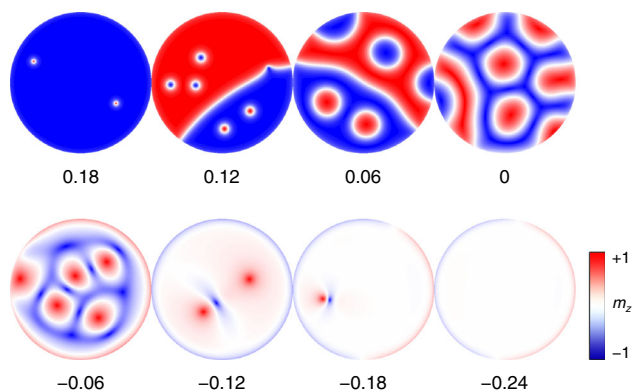


Fig. 3 Evolutions of spin textures under the modulations of magnetic anisotropy. Relaxed magnetic configurations under various K -values.

Fig. 4a, b. We found that J_1 and K increase significantly with the polarization intensity along the $-z$ direction; both reach its maximum at $3P-$, 348 and 449% increase with respect to that of LaCl monolayer, respectively. When the polarization switches to the $+z$ direction, the in-plane exchange interaction parameters J_2 and J_3 have enhanced in the LaCl/3 $P+$ configuration compared to the monolayer LaCl. K decreases gradually with a decreasing polarization, and the easy-axis switches to out-of-plane in the LaCl/3 $P+$ configuration. Therefore, the polarization vector offers a channel via which we may tune the exchange coupling and magnetic anisotropy. As a result of such correlation, the Curie temperature of LaCl shifts with the polarization switching, which is confirmed by the Monte Carlo simulation shown in Fig. 4c. We are thus able to tune the magnetism of the HS from FM LaCl/(3) $P+$ to paramagnetic LaCl/(3) $P-$ by the polarization when the temperature is in the range between 92 K (102 K) and 99 K

(110 K). They discuss the T_c in detail in part 3 of the Supplementary Information. The magnetoelectric coupling in our system is robust and the two FE polarization states are stable: One can be switched into the other by an external electric field, yet either can survive the field removal. This bistability of FE polarization of In $_2$ Se $_3$ means that the magnetic properties of the LaCl layer can be switched steadily between the two states. This feature is highly desirable in nonvolatile information storage.

Moreover, we found that the net magnetic moment is highly correlated with the charge transfer between LaCl and In $_2$ Se $_3$, which is shown in Fig. 4d, e. The decrease in the electron number on the LaCl side is beneficial to the increase in the net magnetic moment of the system. In the LaCl/(3) $P-$ configuration in particular, compared to LaCl/(3) $P+$, more electrons participate in charge transfer to In $_2$ Se $_3$, resulting in a significant increase in the net magnetic moment of the system. As shown in Fig. 5a, the spin-up states in the LaCl/3 $P-$ configuration is populated more than the spin-down state. Viewing the decrease in the electron number on the LaCl side, we are able to conclude that the charge transfer across the interface from LaCl to In $_2$ Se $_3$ occurs mainly in the spin-down state.

The mechanism for interfacial multiferroicity. Change in electronic structure holds the key to understand the variation in magnetism induced by polarization switching. As the differential charge density distribution in Fig. 5c shows, the tuning of the magnetism can be interpreted by electronic reconfiguration that takes place on the LaCl side. In the LaCl/3 $P+$ configuration, pushed “down” by the FE polarization along $+z$, the electrons on the LaCl side are transferred from the top to the bottom surface of the entire HS, shown in Fig. 5b. While in the case of LaCl/3 $P-$, the opposite polarization brings “up” electrons in LaCl from the lower surface. However, unlike the case of LaCl/3 $P+$, electrons

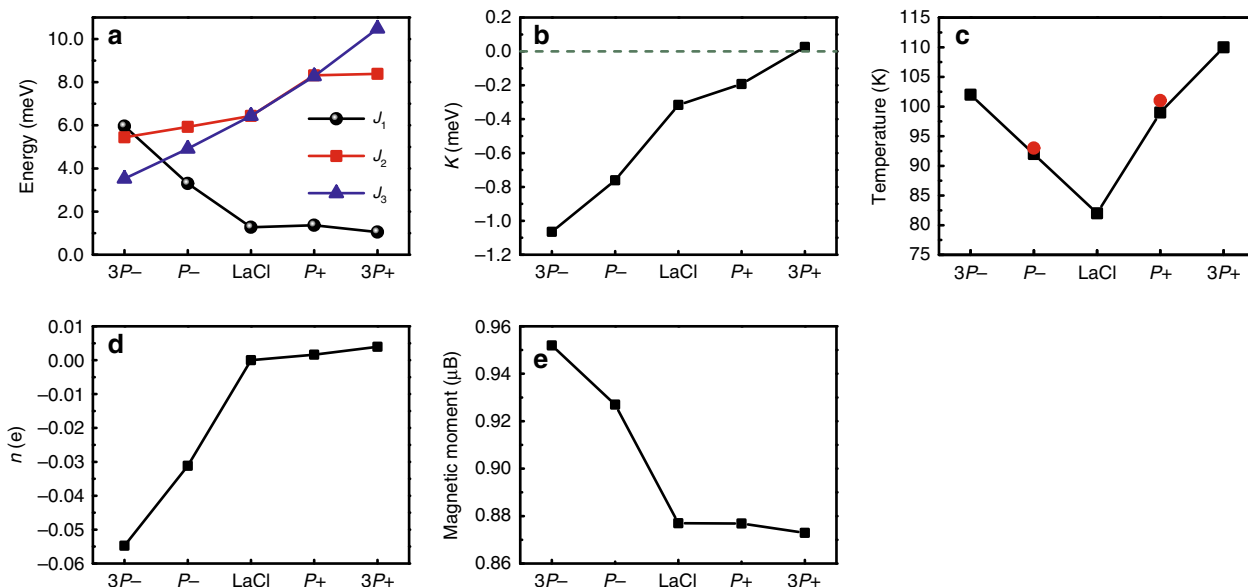


Fig. 4 The influence of polarization intensity on magnetic parameters. **a** Exchange interaction parameters in LaCl. **b** Perpendicular magnetic anisotropy constant in LaCl (**c**) Curie temperature (T_C) of LaCl. Since we only calculated the DMI of LaCl/ P_{\pm} , the effects of the perpendicular magnetic anisotropy and exchange interaction terms on T_C are presented by the data in black squares, and the effect of DMI on T_C in LaCl/ P_{\pm} is presented by the data in red spheres. **d** The number of electrons gained of LaCl. **e** The net magnetic moment of LaCl. In these figures, $3P_{\pm}$ represents a configuration that contains three In_2Se_3 layers.

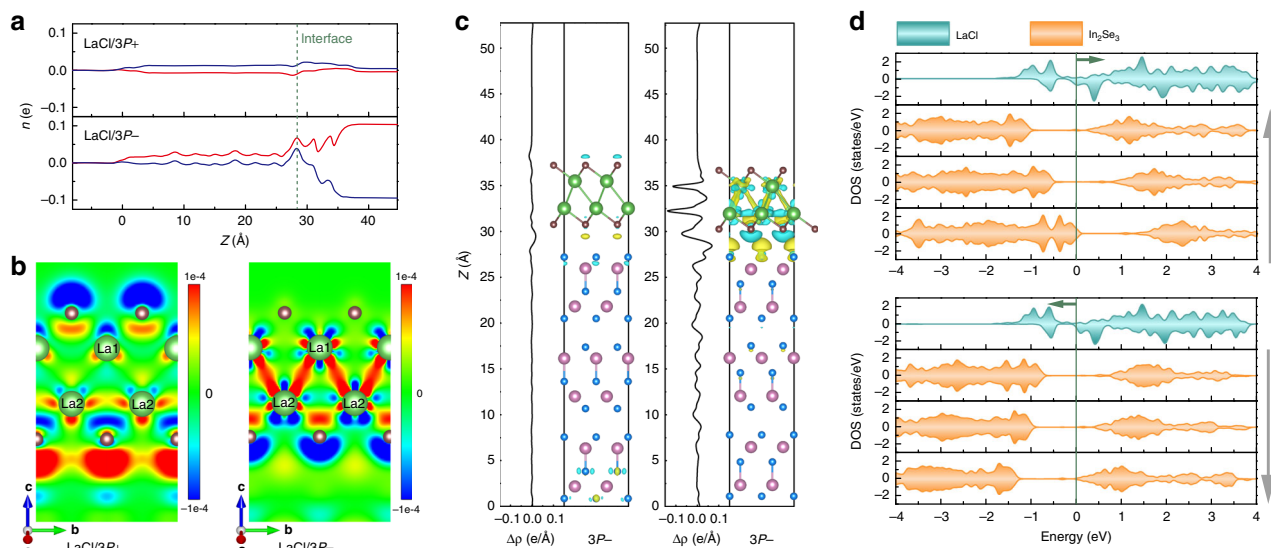


Fig. 5 Charge transfer in different polarization states. **a** Spin-up (red line) and -down (blue line) contributions on the charge transfers in LaCl/ $3P_{\pm}$ HSs. **b** Differential charge density on the LaCl side. **c** Differential charge density distributions of LaCl/ $3P_{\pm}$ HSs and integrals of differential charge densities (black line). **d** The layer-resolved partial DOS of LaCl/ $3P_{\pm}$ HSs. The gray and green arrows represent the polarization direction of In_2Se_3 and the moving direction of Fermi level in HSs, respectively.

are not directly transferred to the upper surface. Instead, it is concentrated in between La1 and La2. Different charge distribution ultimately affects the exchange coupling constant J on the LaCl side, rendering it different in the $3P+$ and $3P-$ states. As per polarization switching, the electrons around the La ion are redistributed, leading to variation in the spin-orbit coupling of the La atom, too. This eventually gives rise to the variation of the DMI on the LaCl side.

We performed a layer-resolved partial density calculation on the LaCl/ $3P_{\pm}$ configurations to scrutinize the underlying mechanism. Figure 5d shows that the electronic distribution on the LaCl side, driven by the built-in electric field of In_2Se_3 ,

remains largely unchanged yet the Fermi energy has been shifted, which is due to the change of electric potential caused by the polarization discontinuity. In addition, owing to the broken time-reversal symmetry in ferromagnetic (LaCl part) materials, the charge transfer between LaCl and In_2Se_3 is different for spin-up and spin-down states, which results in magnetic states change in the two states that are polarized oppositely. The above analysis reveals that the change in ferromagnetism in LaCl is mainly driven by two mechanisms: (i) change in potentials caused by the polarization discontinuity, and (ii) time-reversal symmetry breaking in magnetic materials leads to a difference in charge transfer for spin-up and spin-down states. These two

requirements for polarization tuning of magnetism in HS are not limited to the present LaCl/In₂Se₃ system and we foresee that effective control of 2D ferromagnetism can be realized in other materials, too.

We must nevertheless point out that the surface layer of In₂Se₃ in the LaCl/3P+ configuration exhibits metallic behavior and it falls into the category of polar metal. The screening effect in metal eliminates the possibility of FE switching in bulk materials. This screening is, however, negligible in an atomically thin film due to the strong penetration of the external electric field. The switchable behavior of 2D polar metals has been demonstrated experimentally²⁹. Switching the polarization vector using an external electric field is therefore a viable solution.

In summary, we designed and investigated a 2D vdW LaCl/In₂Se₃ HS. Magnetic skyrmions can exist in bimerons form therein with a diameter of about 23 nm. By switching the polarization in In₂Se₃, the anisotropy, FM Curie temperature, and the bimerons were manipulated. Such a robust magnetoelectric coupling effect that occurs in a 2D vdW HS is unprecedented. Further analysis shows that the coupling between FM and FE is attributed to the effect of the polarization discontinuity in the FE substrate and the broken time-reversal symmetry in the magnetic film. Therefore, such tunability in magnetic properties achieved in the LaCl/In₂Se₃ HS can be transplanted to other material systems, too. The significance of this work is twofold. It not only demonstrates the feasibility of nonvolatile control for magnetism and skyrmions in LaCl/In₂Se₃ HS but also puts forward a general idea to manipulate many characteristics of the 2D vdW HSs by two oppositely polarized states. Furthermore, this work highlights that an artificially designed 2D multiferroic HS is an ideal platform to realize large ME coupling and observe nontrivial physical properties.

Methods

The DFT method and parameters. First-principles calculations were performed using the VASP package based on the projected augmented wave pseudopotentials^{50,51}. The electronic exchange–correlation potential is treated within the spin-polarized generalized gradient approximation plus U (GGA + U) of PBEsol formula^{50,63–65}. Due to that, the GGA algorithm will underestimate the bandgap of the f orbitals, an effective 7 eV Hubbard U_{eff} parameter is applied on La's f orbitals using the Dudarev method⁶⁶ in order to correct its bandgap and prevents f orbitals from participating in orbital hybridization near the Fermi level. We take the van der Waals corrections as parameterized in the semiempirical DFT-D3 method into consideration for all the configurations⁶⁷. The first Brillouin zone is sampled with the $9 \times 9 \times 1$ k -points meshes for the DFT calculation both of the monolayer and the HSs. In order to ensure the energy convergence, denser k -points meshes up to $15 \times 15 \times 1$ are also tested, which shows that $9 \times 9 \times 1$ settings are enough to achieve the desired accuracy. A plane-wave basis set with a kinetic energy cutoff of 500 eV is employed. All structures are fully relaxed until the energy and force converge to 10^{-5} eV and 10^{-2} eV/Å, respectively. To eliminate the periodic boundary effect, a 15 Å thickness vacuum layer is introduced along the z direction. Using spin–orbit coupling for calculating magnetic anisotropic energy and DMI.

OOMMF simulations parameters. OOMMF software were used to simulate the magnetization dynamics⁵². The time evolution of the magnetization is described by the Landau–Lifshitz–Gilbert (LLG) equation⁶⁸.

$$\frac{d\mathbf{M}}{dt} = -\gamma_0 \mathbf{M} \times \mathbf{h}_{\text{eff}} + \alpha \left(\mathbf{M} \times \frac{d\mathbf{M}}{dt} \right), \quad (3)$$

where $\mathbf{h}_{\text{eff}} = -\delta H/\delta \mathbf{M}$ is the effective field, α is the Gilbert damping coefficient, and γ_0 is the absolute gyromagnetic ratio. We include in the simulation a Slonczewski-like spin-transfer torque (STT) driven by the spin current that is generated by the spin-Hall effect,

$$\boldsymbol{\tau} = -\frac{\gamma_0 \hbar j P}{2ae\mu M_s} \mathbf{M} \times (\mathbf{M} \times \mathbf{p}). \quad (4)$$

Parameter e is the electron charge and M_s is the saturation magnetic moment. j is the electric current density. Spin-Hall angle $P = 0.4$. The lattice constant $a = 4$ Å. The polarization of spin current is $\mathbf{p} = -x$. The parameters of LaCl monolayer and LaCl/In₂Se₃ HS are shown in Table 1. In simulations models, we keep $\alpha = 0.2$ and $\gamma_0 = 2.211 \times 10^5$ m A⁻¹ s⁻¹. The size of the cells is chosen to be 4 Å \times 4 Å \times 5 Å.

Data availability

The data that support the findings of this study are available from the corresponding authors upon reasonable request.

Received: 21 May 2020; Accepted: 30 October 2020;

Published online: 23 November 2020

References

- Roessler, U. K., Bogdanov, A. & Pleiderer, C. Spontaneous skyrmion ground states in magnetic metals. *Nature* **442**, 797–801 (2006).
- Mühlbauer, S. et al. Skyrmion lattice in a chiral magnet. *Science* **323**, 915–919 (2009).
- Yu, X. et al. Real-space observation of a two-dimensional skyrmion crystal. *Nature* **465**, 901–904 (2010).
- Birch, M. et al. Real-space imaging of confined magnetic skyrmion tubes. *Nat. Commun.* **11**, 1726 (2020).
- Moreau-Luchaire, C. et al. Additive interfacial chiral interaction in multilayers for stabilization of small individual skyrmions at room temperature. *Nat. Nanotechnol.* **11**, 444–448 (2016).
- Meyer, S. et al. Isolated zero field sub-10 nm skyrmions in ultrathin Co films. *Nat. Commun.* **10**, 3823 (2019).
- Moriya, T. Anisotropic superexchange interaction and weak ferromagnetism. *Phys. Rev.* **120**, 91 (1960).
- Schulz, T. et al. Emergent electrostatics of skyrmions in a chiral magnet. *Nat. Phys.* **8**, 301–304 (2012).
- Zeissler, K. et al. Diameter-independent skyrmion Hall angle observed in chiral magnetic multilayers. *Nat. Commun.* **11**, 428 (2020).
- Jonietz, F. et al. Spin transfer torques in MnSi at ultralow current densities. *Science* **330**, 1648–1651 (2010).
- Zang, J., Mostovoy, M., Han, J. H. & Nagaosa, N. Dynamics of skyrmion crystals in metallic thin films. *Phys. Rev. Lett.* **107**, 136804 (2011).
- Nagaosa, N. & Tokura, Y. Topological properties and dynamics of magnetic skyrmions. *Nat. Nanotechnol.* **8**, 899–911 (2013).
- Maccariello, D. et al. Electrical detection of single magnetic skyrmions in metallic multilayers at room temperature. *Nat. Nanotechnol.* **13**, 233–237 (2018).
- Romming, N. et al. Writing and deleting single magnetic skyrmions. *Science* **341**, 636–639 (2013).
- Yu, X. et al. Current-induced nucleation and annihilation of magnetic skyrmions at room temperature in a chiral magnet. *Adv. Mater.* **29**, 1606178 (2017).
- Ding, B. et al. Observation of magnetic skyrmion bubbles in a van der Waals ferromagnet Fe₃GeTe₂. *Nano Lett.* **20**, 868–873 (2019).
- Park, T.-E. et al. Observation of magnetic skyrmion crystals in a van der Waals ferromagnet Fe₃GeTe₂. Preprint at <https://arxiv.org/abs/1907.01425> (2019).
- Wang, L. et al. Ferroelectrically tunable magnetic skyrmions in ultrathin oxide heterostructures. *Nat. Mater.* **17**, 1087–1094 (2018).
- Huang, B. et al. Layer-dependent ferromagnetism in a van der Waals crystal down to the monolayer limit. *Nature* **546**, 270–273 (2017).
- Gong, C. et al. Discovery of intrinsic ferromagnetism in two-dimensional van der Waals crystals. *Nature* **546**, 265–269 (2017).
- Deng, Y. et al. Gate-tunable room-temperature ferromagnetism in two-dimensional Fe₃GeTe₂. *Nature* **563**, 94–99 (2018).
- Bonilla, M. et al. Strong room-temperature ferromagnetism in VSe₂ monolayers on van der Waals substrates. *Nat. Nanotechnol.* **13**, 289–293 (2018).
- Wang, B. et al. High Curie-temperature intrinsic ferromagnetism and hole doping-induced half-metallicity in two-dimensional scandium chlorine monolayers. *Nanoscale Horiz.* **3**, 551–555 (2018).
- Tan, C. et al. Hard magnetic properties in nanoflake van der Waals Fe₃GeTe₂. *Nat. Commun.* **9**, 1554 (2018).
- Zhang, X. et al. High Curie temperature and intrinsic ferromagnetic half-metallicity in two-dimensional Cr₂X₄ (X = S, Se, Te) nanosheets. *Nanoscale Horiz.* **4**, 859–866 (2019).
- Ding, W. et al. Prediction of intrinsic two-dimensional ferroelectrics in In₂Se₃ and other III 2-VI 3 van der Waals materials. *Nat. Commun.* **8**, 14956 (2017).
- Chang, K. et al. Discovery of robust in-plane ferroelectricity in atomic-thick SnTe. *Science* **353**, 274–278 (2016).
- Liu, F. et al. Room-temperature ferroelectricity in CuInP₂S₆ ultrathin flakes. *Nat. Commun.* **7**, 12357 (2016).
- Fei, Z. et al. Ferroelectric switching of a two-dimensional metal. *Nature* **560**, 336–339 (2018).
- Si, M., Liao, P.-Y., Qiu, G., Duan, Y. & Ye, P. D. Ferroelectric field-effect transistors based on MoS₂ and CuInP₂S₆ two-dimensional van der Waals heterostructure. *ACS Nano* **12**, 6700–6705 (2018).

31. Chandrasekaran, A., Mishra, A. & Singh, A. K. Ferroelectricity, antiferroelectricity, and ultrathin 2D electron/hole gas in multifunctional monolayer MXene. *Nano Lett.* **17**, 3290–3296 (2017).
32. Yin, H., Liu, C., Zheng, G.-P., Wang, Y. & Ren, F. Ab initio simulation studies on the room-temperature ferroelectricity in two-dimensional β -phase GeS. *Appl. Phys. Lett.* **114**, 192903 (2019).
33. Kharkov, Y., Sushkov, O. & Mostovoy, M. Bound states of skyrmions and merons near the Lifshitz point. *Phys. Rev. Lett.* **119**, 207201 (2017).
34. Yu, X. et al. Transformation between meron and skyrmion topological spin textures in a chiral magnet. *Nature* **564**, 95–98 (2018).
35. Kim, S. K. Dynamics of bimeron skyrmions in easy-plane magnets induced by a spin supercurrent. *Phys. Rev. B* **99**, 224406 (2019).
36. Zhao, Y., Zhang, J. J., Yuan, S. & Chen, Z. Nonvolatile electrical control and heterointerface-induced half-metallicity of 2D ferromagnets. *Adv. Funct. Mater.* **29**, 1901420 (2019).
37. Gong, C., Kim, E. M., Wang, Y., Lee, G. & Zhang, X. Multiferroicity in atomic van der Waals heterostructures. *Nat. Commun.* **10**, 2657 (2019).
38. Sun, W., Wang, W., Chen, D., Cheng, Z. & Wang, Y. Valence mediated tunable magnetism and electronic properties by ferroelectric polarization switching in 2D Fe₂/In₂Se₃ van der Waals heterostructures. *Nanoscale* **11**, 9931–9936 (2019).
39. Cui, C. et al. Intercorrelated in-plane and out-of-plane ferroelectricity in ultrathin two-dimensional layered semiconductor In₂Se₃. *Nano Lett.* **18**, 1253–1258 (2018).
40. Xue, F. et al. Multidirection piezoelectricity in mono- and multilayered hexagonal α -In₂Se₃. *ACS Nano* **12**, 4976–4983 (2018).
41. Li, W. et al. Large disparity between optical and fundamental band gaps in layered In₂Se₃. *Phys. Rev. B* **98**, 165134 (2018).
42. Araujo, R. E. & Corbett, J. D. Lanthanum monochloride and lanthanum sesquichloride. *Inorg. Chem.* **20**, 3082–3086 (1981).
43. Mattausch, H., Simon, A., Holzer, N. & Eger, R. Monohalogenide der Lanthanoide [1]. *Z. Anorg. Allg. Chem.* **466**, 7–22 (1980).
44. Meyer, G. Reduced halides of the rare-earth elements. *Chem. Rev.* **88**, 93–107 (1988).
45. Corbett, J. D. Extended metal-metal bonding in halides of the early transition metals. *Acc. Chem. Res.* **14**, 239–246 (1981).
46. Wu, M. High-temperature intrinsic quantum anomalous Hall effect in rare Earth monohalide. *2D Mater.* **4**, 021014 (2017).
47. Liu, Z. et al. Intrinsic quantum anomalous hall effect with in-plane magnetization: searching rule and material prediction. *Phys. Rev. Lett.* **121**, 246401 (2018).
48. Nie, S., Weng, H. & Prinz, F. B. Topological nodal-line semimetals in ferromagnetic rare-earth-metal monohalides. *Phys. Rev. B* **99**, 035125 (2019).
49. Jiang, Z., Wang, P., Xing, J., Jiang, X. & Zhao, J. Screening and design of novel 2D ferromagnetic materials with high Curie temperature above room temperature. *ACS Appl. Mater. Interfaces* **10**, 39032–39039 (2018).
50. Perdew, J. P., Burke, K. & Ernzerhof, M. Generalized gradient approximation made simple. *Phys. Rev. Lett.* **77**, 3865 (1996).
51. Kresse, G. & Furthmüller, J. Efficient iterative schemes for ab initio total-energy calculations using a plane-wave basis set. *Phys. Rev. B* **54**, 11169 (1996).
52. Donahue, M. J. & Porter, D. G. *OOMMF User's Guide Interagency Report NISTIR 6376* (National Institute of Standards and Technology, Gaithersburg, MD, 1999).
53. Rohart, S. & Thiaville, A. Skyrmion confinement in ultrathin film nanostructures in the presence of Dzyaloshinskii-Moriya interaction. *Phys. Rev. B* **88**, 184422 (2013).
54. Zhang, X., Zhou, Y. & Ezawa, M. Magnetic bilayer-skyrmions without skyrmion Hall effect. *Nat. Commun.* **7**, 10293 (2016).
55. Tang, W., Sanville, E. & Henkelman, G. A grid-based Bader analysis algorithm without lattice bias. *J. Phys.: Condens. Matter* **21**, 084204 (2009).
56. Sanville, E., Kenny, S. D., Smith, R. & Henkelman, G. Improved grid-based algorithm for Bader charge allocation. *J. Comput. Chem.* **28**, 899–908 (2007).
57. Henkelman, G., Arnaldsson, A. & Jónsson, H. A fast and robust algorithm for Bader decomposition of charge density. *Comput. Mater. Sci.* **36**, 354–360 (2006).
58. Dzyaloshinsky, I. A thermodynamic theory of “weak” ferromagnetism of antiferromagnetics. *J. Phys. Chem. Solids* **4**, 241–255 (1958).
59. Liu, J., Shi, M., Lu, J. & Anantram, M. Analysis of electrical-field-dependent Dzyaloshinskii-Moriya interaction and magnetocrystalline anisotropy in a two-dimensional ferromagnetic monolayer. *Phys. Rev. B* **97**, 054416 (2018).
60. Moon, K.-W., Yoon, J., Kim, C. & Hwang, C. Existence of in-plane magnetic skyrmion and its motion under current flow. *Phys. Rev. Appl.* **12**, 064054 (2019).
61. Jiang, W. et al. Direct observation of the skyrmion Hall effect. *Nat. Phys.* **13**, 162–169 (2017).
62. Zhao, W. et al. Magnetic proximity and nonreciprocal current switching in a monolayer WTe₂ helical edge. *Nat. Mater.* **19**, 503–507 (2020).
63. Kresse, G. & Joubert, D. From ultrasoft pseudopotentials to the projector augmented-wave method. *Phys. Rev. B* **59**, 1758 (1999).
64. Blöchl, P. E. Projector augmented-wave method. *Phys. Rev. B* **50**, 17953 (1994).
65. Perdew, J. P. et al. Restoring the density-gradient expansion for exchange in solids and surfaces. *Phys. Rev. Lett.* **100**, 136406 (2008).
66. Dudarev, S., Botton, G., Savrasov, S., Humphreys, C. & Sutton, A. Electron-energy-loss spectra and the structural stability of nickel oxide: an LSDA+ U study. *Phys. Rev. B* **57**, 1505 (1998).
67. Grimme, S., Antony, J., Ehrlich, S. & Krieg, H. A consistent and accurate ab initio parametrization of density functional dispersion correction (DFT-D) for the 94 elements H-Pu. *J. Chem. Phys.* **132**, 154104 (2010).
68. Landau, L. D. & Lifshitz, E. On the theory of the dispersion of magnetic permeability in ferromagnetic bodies. *Phys. Z. Sowjetunion* **8**, 153 (1935).

Acknowledgements

We acknowledge grants from the National Natural Science Foundation of China under research (Nos. 51571083 and 11674083) and the Foundation of Postgraduate Education Innovation and Quality Improvement Project of Henan University (No. CX3040A0920215). Z.X.C. thanks Australia Research Council for support (DP190100150). H.L. acknowledges the support from the National Natural Science Foundation of China (Grant No. 11804078) and Henan University (Grant No. CJ3050A0240050).

Author contributions

Z.X.C. conceived the idea. W.S., Z.X.C., and H.L. carried out the calculation and analysis of the result. W.S., Z.X.C., and H.L. wrote the paper. All authors contribute the comments on the paper.

Competing interests

The authors declare no competing interest.

Additional information

Supplementary information is available for this paper at <https://doi.org/10.1038/s41467-020-19779-6>.

Correspondence and requests for materials should be addressed to H.L. or Z.C.

Peer review information *Nature Communications* thanks the anonymous reviewer(s) for their contribution to the peer review of this work. Peer reviewer reports are available.

Reprints and permission information is available at <http://www.nature.com/reprints>

Publisher's note Springer Nature remains neutral with regard to jurisdictional claims in published maps and institutional affiliations.



Open Access This article is licensed under a Creative Commons Attribution 4.0 International License, which permits use, sharing, adaptation, distribution and reproduction in any medium or format, as long as you give appropriate credit to the original author(s) and the source, provide a link to the Creative Commons license, and indicate if changes were made. The images or other third party material in this article are included in the article's Creative Commons license, unless indicated otherwise in a credit line to the material. If material is not included in the article's Creative Commons license and your intended use is not permitted by statutory regulation or exceeds the permitted use, you will need to obtain permission directly from the copyright holder. To view a copy of this license, visit <http://creativecommons.org/licenses/by/4.0/>.

© The Author(s) 2020